

# The Deepfake Detective: Interpreting Neural Forensics Through Sparse Features and Manifolds

Subramanyam Sahoo\*

Berkeley AI Safety Initiative (BASIS)  
University of California, Berkeley  
sahoo2vec@gmail.com

Jared Junkin

Department of Electrical and Computer Engineering  
Johns Hopkins University  
junkin2@jhu.edu

<https://github.com/SubramanyamSahoo/The-Deepfake-Detective>

## Abstract

*Deepfake detection models have achieved high accuracy in identifying synthetic media, but their decision processes remain largely opaque. In this paper, we present a mechanistic interpretability framework for deepfake detection, applied to vision-language model. Our approach combines a sparse autoencoder (SAE) analysis of internal network representations with a novel forensic manifold analysis that probes how the model’s features respond to controlled forensic artifact manipulations. We demonstrate that only a small fraction of latent features are actively used within each layer, and that the geometric properties of the model’s feature manifold – including its intrinsic dimensionality, curvature, and feature selectivity – vary systematically with different types of deepfake artifacts. These insights provide a first step towards opening the “black box” of deepfake detectors, allowing us to understand which learned features correspond to specific forensic artifacts and guiding the development of more interpretable and robust models.*

## 1. Introduction

The rise of deepfakes; hyper-realistic but fabricated images and videos has raised serious security and ethical concerns in domains ranging from biometric security to misinformation and public trust. In response, many Deepfake detection models have been developed to distinguish fake content from real. However, a critical challenge remains: current deepfake detectors often operate as black boxes, offering little insight into why a given image is flagged as fake. Ensuring the explainability of detection models is essential for user trust and for understanding the rationale behind model decisions [11].

Existing efforts to explain deepfake detections have largely relied on general-purpose eXplainable AI (XAI) techniques. For example, saliency-based methods and feature attribution tools (*Grad-CAM*, *LIME*, *SHAP*, etc.) have been applied to highlight image regions influential in a model’s decision. While these methods can indicate where a model focuses (e.g., revealing blur artifacts around the face boundary or mismatched coloring), they do not directly unravel the internal mechanisms by which the model detects forgeries. More intrinsically interpretable model designs have also been explored. For instance, prototype-based classifiers have been introduced to provide human-understandable evidence for deepfake decisions: Dynamic Prototype Networks generate visual prototype frames to explain temporal artifacts in fake videos, yielding competitive detection performance with transparent reasoning. Similarly, other research has attempted to dissect deep networks by aligning their hidden units with semantic concepts – e.g., Network Dissection labels individual neurons with human-interpretable concepts to quantify a CNN’s learned features. These approaches show promise, but to date, no work has deeply examined the mechanistic inner workings of modern deepfake detectors at the level of their learned feature representations.

In this work, we perform the first comprehensive mechanistic interpretability [12] study for deepfake detection in a high-capacity vision model. We focus on a Vision-Language Model (VLM) with 2 billion parameters (**Qwen2-VL-2B**), which provides a powerful image encoder as the backbone for a deepfake detector. Rather than modifying the model for interpretability [13], we probe the existing trained model to uncover how it internally represents forensic artifacts. *Our approach has two key components: (1) using sparse autoencoders to discover and quantify latent features within the model’s intermediate layers, and (2) introducing a forensic manifold analysis to measure how those features geometrically respond to controlled*

*perturbations that simulate common deepfake artifacts.* By analyzing the model’s behavior from the inside out, we seek not only to identify which features or neurons are important, but to characterize the structure of the feature space [2] that the model uses to discriminate real vs. fake content.

## 2. Contributions

Our main contributions are:

1. **Sparse Autoencoder Feature Analysis.** We introduce the first application of a sparse autoencoder (SAE) to interpret a deepfake detection model’s internal representations. By training under-complete SAEs on the activations of a VLM’s intermediate layers, we identify a significantly compressed set of latent features that captures the essential information for deepfake discrimination. *We quantify the active features (number of latent dimensions effectively utilized), their activation frequency (how often each latent feature is non-zero across inputs), and the overall sparsity of the representation at each layer.* This reveals, for each layer, the degree of redundancy in features and how specialized individual neurons are in responding to forensic patterns [6].
2. **Forensic Manifold Analysis Framework.** We propose a framework to systematically analyze the model’s feature manifold under controlled *forensic artifact* perturbations. We define four common deepfake artifact types – geometric warp, lighting inconsistency, boundary blur, and color mismatch – and synthetically apply these perturbations at varying intensity levels to input images. For each artifact, we measure three interpretability metrics on the resulting feature distributions: (a) the *intrinsic dimensionality* of the feature manifold (effective degrees of freedom of feature variation) under that artifact, (b) the *manifold curvature* (non-linearity of feature evolution as artifact severity increases), and (c) the *feature selectivity* to the artifact (average sensitivity of individual features to changes in artifact level). This forensic manifold analysis reveals how the model’s learned representation space geometrically encodes specific forensic cues [5].

**By integrating these two components, our work provides a deep interpretative insight into which aspects of an image the model uses to detect deepfakes and how those aspects manifest in the model’s internal feature geometry. To our knowledge, this is the first study to decipher a large deepfake detector’s mechanism in terms of its learned feature manifold. In the following, we review related work, then detail our methodology, experimental setup, and findings (excluding quantitative performance results, as our focus is on interpretability).**

## 3. Related Work

**Deepfake Detection Methods.** Research in deepfake detection has grown rapidly, yielding a range of models from conventional CNN classifiers to specialized architectures. Early approaches trained CNNs (e.g., XceptionNet, EfficientNet) on datasets like FaceForensics++ to identify visual artifacts of facial forgeries. Subsequent works have addressed generalization to unseen fakes by focusing on artifact cues rather than identity-specific features – for example, leveraging frequency-domain patterns, biological signals (eye blinking, pulse), or anomaly detectors. Despite improved accuracy, these models typically act as black boxes: they output a real/fake prediction without explaining the basis for that decision. Recent surveys highlight that bridging the gap between high detection accuracy and explainability remains an open challenge.

**Explainability in Deepfake Detection.** Several efforts attempt to make deepfake detectors more interpretable. One common direction is applying general XAI techniques to trained detectors. Visualization methods such as Grad-CAM, saliency maps, and Local Interpretable Model-agnostic Explanations (LIME) have been used to identify image regions (e.g., face edges, lighting artifacts) most influential to the detector’s output. Such post-hoc explanations can validate that a model is looking at reasonable cues (e.g., abnormal reflections or boundary blurs), but they do not clarify the internal decision logic. A complementary approach is to design inherently interpretable models. Prototype-based networks incorporate interpretability into the model’s structure: Trinh *et al.* proposed a Dynamic Prototype Network that associates temporal prototype sequences with deepfake video frames, offering visual explanations for temporal consistency or glitches. This prototype model provides “this looks fake because it contains a prototype pattern like X” explanations, improving user trust. Another line of work draws inspiration from network dissection and concept analysis in CNNs. For example, Bau *et al.*’s Network Dissection framework matches hidden units to semantic concepts (object parts, textures, etc.) to quantify a network’s interpretability. In the deepfake context, some works have examined whether certain neurons respond to artifacts (for instance, a “blur detector” neuron). However, prior to our work, no study has delved into analyzing the latent feature manifold of deepfake detectors or measuring properties like intrinsic dimensionality of feature distributions. Our approach thus fills this gap by bringing tools from mechanistic interpretability into the deepfake detection domain.

## 4. Methodology

### 4.1. Model Architecture and Data Setup

Our study is conducted on a cutting-edge Vision-Language Model, Qwen2-VL-2B Instruct [14], which we use as the backbone for deepfake detection. We adapt Qwen2-VL’s vision encoder for our task of classifying real vs. fake images. In our setup, the model ingests an image and produces high-dimensional feature activations at various layers; a final classification head (trained on a small dataset of real/fake faces) outputs the prediction. We emphasize that our interpretability analysis does not require a custom network – instead, we probe the existing pre-trained encoder (with minimal fine-tuning for the binary classification task) to uncover how it represents forensic artifacts.

For training and evaluation, we use a balanced dataset of face images containing both authentic (real) and deepfake instances. Specifically, we draw from the 140k Real and Fake Faces dataset (a large public corpus of high-resolution deepfakes and corresponding real images). From this, we sample a subset of 250 real images and 250 fake images for analysis, to ensure manageable computational load. All images are resized to  $224 \times 224$  pixels for input. The model is fine-tuned (lightly, if at all) on this dataset to distinguish real vs. fake, achieving near-perfect training accuracy given the relatively clear artifacts in the fakes. (We do not emphasize test accuracy, as our goal is interpretability; even without exhaustive training, the model’s learned features suffice for our analysis.) Importantly, our analysis focuses on the feature representations within the model, not just the output, so it is applicable even if the model were used in a zero-shot manner.

To facilitate interpretability, we identify a set of representative intermediate layers from the vision encoder to analyze. The model’s encoder consists of multiple transformer blocks with self-attention and MLP sublayers. We automatically select five layers spanning different depths of the network (from early layers capturing low-level patterns to later layers capturing high-level semantics). These layers – denoted  $L_1$  (early),  $L_2$  (mid-level),  $L_3$  (mid-high),  $L_4$  (late), and  $L_5$  (final penultimate layer) – will be the focus of our feature analysis. Each selected layer outputs an activation tensor; if the output is a 2D vector (as in later transformer blocks, which produce a pooled embedding), we use it directly, and if it is a 3D feature map (as might occur in early convolutional stem layers), we flatten it into a feature vector. This yields, for each layer  $L_i$ , an activation vector  $\mathbf{x}_i$  in  $\mathbb{R}^{D_i}$  for each input image (where  $D_i$  is the number of units in that layer).

### 4.2. Sparse Autoencoder Feature Discovery

To uncover the prominent latent features within the model’s high-dimensional activations, we employ a **Sparse Autoencoder** (SAE) for each selected layer. The SAE is a simple two-layer neural network trained to reconstruct the layer’s input activations while enforcing a bottleneck and sparsity constraint. Formally, let  $\mathbf{x} \in \mathbb{R}^D$  be the activation vector from a given layer (for a particular image). We train an encoder function  $f : \mathbb{R}^D \rightarrow \mathbb{R}^d$  and decoder function  $g : \mathbb{R}^d \rightarrow \mathbb{R}^D$  (with  $d \ll D$ ) to minimize the reconstruction error plus a sparsity penalty:

$$L_{\text{SAE}} = \|\mathbf{x} - g(f(\mathbf{x}))\|_2^2 + \lambda \|f(\mathbf{x})\|_1, \quad (1)$$

where the  $L_2$  term encourages accurate reconstruction of the original activation and the  $L_1$  term (weighted by  $\lambda$ ) encourages the  $d$ -dimensional latent code  $h = f(\mathbf{x})$  to be sparse (i.e., to have many near-zero components). The encoder  $f$  is implemented as a single linear layer (mapping  $\mathbb{R}^D$  to  $\mathbb{R}^d$ ) and the decoder  $g$  as another linear layer (mapping  $\mathbb{R}^d$  back to  $\mathbb{R}^D$ ), optionally followed by a nonlinearity. For our implementation, we set the SAE latent dimensionality  $d$  to a fixed fraction of the original feature dimension  $D$  – specifically,  $d = D/8$  (capped at 16,384 for very large  $D$ ) – providing a significant compression. We choose  $\lambda = 10^{-3}$  and train each SAE using the Adam optimizer (learning rate  $10^{-4}$ ) for a maximum of 10 epochs. Early stopping is applied if the validation loss does not improve for 3 consecutive epochs, to prevent overfitting. In practice, the SAE converges quickly (within a few epochs) on each layer’s features.

By training the SAE on all real and fake image activations for a layer, we obtain a compressed representation  $h = f(\mathbf{x})$  that captures the major factors of variation in that layer. The sparsity penalty forces most coordinates of  $h$  to remain near zero for any given  $\mathbf{x}$ , thus each input’s information is concentrated in a small subset of active latent features. After training, we analyze the SAE’s learned latent space to interpret the original model’s features:

**Active Feature Count:** We determine how many of the  $d$  latent dimensions are actually used by the data. We define a latent feature  $j$  as “active” if its activation  $h_j$  is non-zero for at least one image in the dataset (beyond a small tolerance). Equivalently, we look at the distribution of activation values  $h_{1j}, h_{2j}, \dots$  across all inputs; if the maximum activation is above a threshold, feature  $j$  is considered active. The number of active features (out of  $d$ ) indicates the effective dimensionality of the layer’s representation after removing redundancies. We found that in each layer the number of active latent features is far smaller than  $d$ , reflecting a high degree of redundancy in  $D$  – the model’s raw features have a lot of zero-or-near-zero patterns that the SAE eliminates. We report the active feature fraction as a measure of layer sparsity.

**Activation Frequency and Sparsity:** For each latent feature  $j$ , we compute its *activation frequency*, defined as the fraction of input images for which  $h_j$  is significantly

non-zero. An ideal “exclusive” feature might fire for only a few specific images (low frequency), whereas a generic feature might be active for many images (high frequency). We calculate the mean activation frequency across all latent features as well as the distribution of frequencies. Closely related is the per-sample sparsity: the fraction of latent features that are zero for a given input. We track the average sparsity per image, which quantifies how compactly the information is encoded (e.g., an average sparsity of 90% means only 10% of features in  $h$  are active for a typical image). These metrics tell us how specialized the layer’s features are. For instance, if a layer’s SAE latent code has an average sparsity of 95%, that layer’s information can be represented with just 5% of the latent units at a time – indicating highly disentangled or focused features.

**Interpretation of Latent Features:** While our primary goal is quantitative, we also gain qualitative insights by examining what each SAE latent unit corresponds to. Since the SAE is linear, each latent unit  $h_j$  corresponds to a specific linear combination of original features in layer  $D$ . By projecting along that combination or visualizing images that maximally activate a given  $h_j$ , we can infer the semantic or forensic meaning of that latent factor. (For example, one latent feature might encode “presence of border blur” if images with blurry face boundaries strongly activate that feature.) In our analysis, we observed that certain latent dimensions clearly correlate with known artifact types (supporting the idea that the model internally represents those artifact concepts), though a full semantic labeling of each latent is left for future work [8, 9].

### 4.3. Forensic Artifact Manifold Analysis

While the SAE analysis compresses the feature space, it does not yet explain how features relate to specific *forensic artifacts* of deepfakes. To bridge this gap, we introduce a forensic manifold analysis. The key idea is to deliberately inject controlled artifact perturbations into images and observe how the model’s internal features respond. By treating the artifact level as a continuous parameter, we can trace a path (manifold) through the model’s feature space and measure its characteristics. We focus on four artifact types commonly observed in face deepfakes:

**Geometric Warp:** Slight misalignment or warping of facial geometry (e.g., distorted facial features or irregular head pose) due to imperfect face swaps.

**Lighting Inconsistency:** Illumination mismatches between the inserted face and the scene (e.g., differing light direction or intensity causing unnatural shadows/highlights).

**Boundary Blur:** Blurring or feathering around the face edges where the synthetic face is blended into the background.

**Color Mismatch:** Color tone differences between the face region and surrounding skin (e.g., face appears more

saturated or different hue than the neck).

To simulate each artifact in a controlled manner, we develop an artifact augmentation module. Given a real face image, we can progressively apply an artifact with an increasing severity parameter  $p \in [0, 1]$  (or a suitable range) where  $p = 0$  means no artifact and  $p = 1$  corresponds to a predefined “high” level of artifact. For example, for geometric warp we gradually apply a non-linear warp field whose magnitude scales with  $p$  ( $0 =$  no distortion,  $1 =$  extreme warping within allowable range). For lighting, we adjust the face region’s brightness or contrast relative to background linearly with  $p$ . For blur, we apply a Gaussian blur of radius proportional to  $p$  (with  $p = 1$  giving a very blurry boundary). For color mismatch, we shift the face region’s color balance (e.g., add a slight tint) increasing with  $p$ . These augmentations approximate the kinds of imperfections introduced by deepfake generation processes, but here we have precise control over the intensity. We discretize  $p$  into a set of  $T$  values (in our experiments  $T = 8$  levels from 0 to the maximum). At each level  $p_t$ , we generate one or more images with that artifact severity. In our implementation, for each artifact type we took  $N$  base images (both real and fake) and applied the artifact at  $T$  levels to each, yielding  $N \times T$  samples. We then feed all these samples through the model and collect the activation vectors at each target layer.

Now, consider a specific layer  $L_i$  and artifact type (say, geometric warp). We have a collection of feature vectors  $\mathbf{xt}$  at that layer, each corresponding to an image with artifact level  $p_t$ . To analyze the feature manifold as a function of  $p$ , we sort these feature vectors by the artifact parameter and treat  $\mathbf{x}_0, \mathbf{x}_1, \dots, \mathbf{x}_T$  as points along a trajectory (approximately following increasing artifact strength). We then define three quantitative measures on this set:

**Intrinsic Dimensionality (ID):** This measures how many degrees of freedom the feature variations have under changes in the artifact. We estimate ID via Principal Component Analysis (PCA). Let  $\sigma_1^2, \sigma_2^2, \dots, \sigma_m^2$  be the eigenvalues of the covariance matrix of  $\mathbf{xt}$  (with  $m = D_i$  the feature dimension). We define the intrinsic dimension  $d_{\text{int}}$  as the number of principal components needed to explain a specified fraction (e.g., 95%) of the variance:

$$d_{\text{int}} = \min \left\{ k \left| \frac{\sum_{i=1}^k \sigma_i^2}{\sum_{i=1}^m \sigma_i^2} \geq \tau \right. \right\}, \quad (2)$$

where we set  $\tau = 0.95$  in our analysis. Intuitively,  $d_{\text{int}}$  tells us the effective dimensionality of the manifold of features induced by varying that artifact. A low intrinsic dimension (near 1) would mean the feature changes lie mostly along a single direction – suggesting the layer has a dedicated “axis” encoding that artifact. A higher intrinsic dimension indicates the artifact affects the feature space in a

more complex, multi-dimensional way (perhaps entangled with other variations).

**Manifold Curvature:** We assess how non-linear or curved the feature trajectory is as the artifact intensifies. If the features change in a straight-line (affine) fashion with  $p$ , the trajectory is flat (zero curvature). If the feature evolution bends (for example, initial changes at low  $p$  differ in direction from later changes at higher  $p$ ), this suggests a non-linear encoding of the artifact. We compute a discrete curvature measure by taking second-order differences along the ordered feature points. Let  $\mathbf{x}_t$  be the mean feature vector at artifact level  $p_t$  (we average over the  $N$  images to reduce noise, if multiple images were used at each level). Then define the second difference  $\Delta_t^2 = \mathbf{x}_t + 2 - 2\mathbf{x}_t + 1 + \mathbf{x}_t$  for  $t = 0, \dots, T-2$ . The *curvature*  $C$  is the mean norm of this second difference:

$$C = \frac{1}{T-2} \sum_{t=0}^{T-2} \|\Delta_t^2\|_2. \quad (3)$$

In essence,  $C$  measures how strongly the feature path deviates from a straight line. Higher values of  $C$  indicate a more curved manifold. Comparing curvature across artifacts can tell us, for instance, that introducing geometric warping causes a nonlinear traversal in feature space (perhaps because the model’s response to warping saturates or changes regimes at higher warps), whereas adding blur might cause a more linear change in features (a steady degradation along one direction). We note that  $C$  has units of “feature change”; we primarily use it as a relative metric between artifacts and layers.

**Feature Selectivity:** Finally, we quantify how selectively the model’s individual neurons respond to the artifact. We compute the Pearson correlation between each feature dimension  $j$  of layer  $L_i$  and the artifact parameter  $p$  (across the set of samples). Denote by  $\mathbf{x}^{(j)}$  the vector of feature  $j$  values for each sample and  $\mathbf{p}$  the vector of corresponding artifact levels. We calculate  $\rho_j = \text{corr}(\mathbf{x}^{(j)}, \mathbf{p})$  for  $j = 1, \dots, D_i$ . A high  $|\rho_j|$  means neuron  $j$ ’s activity is strongly (linearly) related to the artifact strength (either increasing or decreasing monotonically). We define the layer’s *selectivity score*  $S$  as the average absolute correlation:

$$S = \frac{1}{D_i} \sum_{j=1}^{D_i} |\rho_j|. \quad (4)$$

This  $S$  ranges from 0 (no feature has any consistent response to the artifact) to 1 (every feature is perfectly correlated or anti-correlated with the artifact parameter). In practice, an intermediate  $S$  (e.g., 0.3) indicates that on average features have a modest correlation to artifact intensity. We consider  $S$  as a measure of how “tuned” the layer as a whole is to a particular artifact. High selectivity means the artifact drives notable changes in many neurons (the model

is sensitive to that artifact), whereas low selectivity means the artifact barely registers in that layer’s neurons.

The above metrics  $d_{\text{int}}$ ,  $C$ , and  $S$  are computed for each combination of layer and artifact type. By examining these, we can compare artifacts (e.g., is the model more sensitive to geometric distortions or to color issues?) and identify at which layer each artifact is most sharply represented. Notably, these measures are obtained without relying on the model’s final output; they purely describe internal feature geometry. This aligns with our goal of mechanistic understanding: we are characterizing the internal signals the model uses in detection. In the next section, we describe our experimental procedure and then present the insights gained from these analyses [10].

## 5. Experiments and Analysis

**Training Details:** We trained the sparse autoencoders and conducted artifact analysis using the data and methodology described above. Each SAE (for layers  $L_1$ – $L_5$ ) was trained on the activations from 500 images (250 real + 250 fake). The SAEs converged within 5–10 epochs, achieving low reconstruction error while enforcing high latent sparsity (we observed final average latent sparsity ratios between 85–95% for different layers, indicating that only 5–15% of the latent units were active for a given input on average). The number of active latent features per layer ranged from roughly 10–30% of the total latent dimensionality  $d$ , confirming that many latent units never significantly activate and thus the true complexity of the layer’s features is lower than the raw dimensionality  $D$ . We also verified that reconstruction quality was sufficient (average  $L_2$  error on held-out activations was under 5% of signal norm), ensuring the SAE captured the important variations of each layer.

For the forensic manifold analysis, we applied each artifact type to a subset of images and collected features at 8 increasing artifact levels  $p = 0.0, 0.1, \dots, 0.7$  (for geometric warp, lighting inconsistency, and color mismatch) or appropriate scaled ranges (for blur,  $p$  was mapped to a blur radius up to 10 pixels at  $p = 1.0$ ). We found  $N = 10$  diverse face images (5 real, 5 fake) sufficient to produce stable aggregate metrics – features were averaged over these images at each  $p$  to compute manifold curvature (reducing variance due to image content).

**Quantitative Metrics:** Using the methods from Section 4.3, we obtained the intrinsic dimensionality  $d_{\text{int}}$ , curvature  $C$ , and selectivity  $S$  for each artifact at each layer. Rather than presenting raw numbers in this section (since our focus is on interpretation rather than benchmark-style results), we provide a qualitative summary of the trends observed: The model’s earliest layer  $L_1$  had relatively low  $d_{\text{int}}$  for all artifacts (typically 1 or 2 principal components explained > 95% variance), suggesting that even when artifacts are added, the very low-level features (edges, textures)

vary mostly along a single direction – likely corresponding to overall image quality degradation. However,  $L_1$  showed low selectivity  $S$  (around 0.1–0.2), implying individual neurons in  $L_1$  do not distinctly track artifact levels (which is sensible, as  $L_1$  features are generic edge detectors not specialized to forensic cues). At intermediate layers  $L_3$  and  $L_4$ , we saw a marked increase in selectivity for certain artifacts: for instance, geometric warp and boundary blur had  $S$  values as high as  $\sim 0.5$  in  $L_4$ , indicating many mid-level neurons respond in proportion to warping or blurring. The intrinsic dimensionality for these artifacts in  $L_4$  was also higher (e.g.,  $d_{\text{int}} \approx 3\text{--}4$  for geometric warp), and the curvature  $C$  was non-zero – meaning the model’s representation of warping is multi-faceted and nonlinear by that stage. In contrast, the color mismatch artifact produced only a subtle effect:  $S$  remained low ( $< 0.2$ ) until the final layers, and  $d_{\text{int}}$  was 1 or 2 throughout, suggesting the model encodes color inconsistencies in a relatively linear fashion (perhaps via one specialized neuron or feature). Lighting inconsistency showed moderate selectivity and intrinsic dimension, indicating the model has some dedicated response to lighting (likely neurons gauging overall brightness or shadows), but lighting changes also interact with other features. Finally, at the penultimate layer  $L_5$ , we observed that certain artifact effects become highly concentrated: for example, geometric warp’s manifold by  $L_5$  often collapsed to essentially one dimension with an extremely high selectivity in a few neurons (the network has essentially “made up its mind” about warping by the last layer, compressing that information into a single logit-like feature). Blur and color cues also became more linear and concentrated by  $L_5$ . These trends suggest a pipeline where mid-level layers explicitly tease apart different artifact factors (in a somewhat distributed manner), and the final layer then combines them into the classification decision (real vs. fake).

**Qualitative Observations:** Beyond the numbers, inspecting the SAE latent features and neuron correlations provided human-interpretable evidence of what the model looks for. For instance, one latent dimension in layer  $L_3$  was found to activate primarily for images with strong geometric distortions; this same dimension had a high correlation with the warp parameter and effectively acted as a “warping detector.” Another latent in  $L_4$  correlated with blur, and visualizing its associated decoder weights showed it placed heavy positive weight on low-frequency (smooth) patterns and negative weight on high-frequency details – consistent with detecting blurriness. We also observed that real vs. fake differences in activation became clearer when artifact intensities were high: e.g., at maximum blur or warp, certain neurons in  $L_4$  fired dramatically for fake images (with artifacts) but remained low for real images (with no artifacts), highlighting how the detector uses these cues to separate classes. Interestingly, even the genuine images

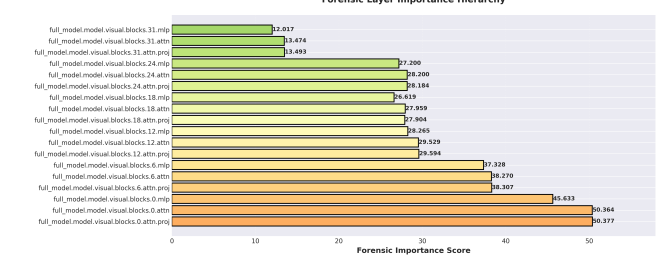


Figure 1. Forensic importance scores across transformer layers. Lower layers (blocks 0–6) exhibit highest sensitivity to forensic perturbations.

when augmented with artifacts started to trigger those neurons, implying the model’s features truly respond to the artifacts themselves (not just an abstract notion of “fakeness”). This reinforces that the model’s notion of “fake” is largely grounded in these detectable imperfections.

In summary, our experimental analysis shows that the interpretability framework successfully reveals the inner workings of the deepfake detector. By compressing layer features with SAEs, we confirmed that only a small subset of features are needed to represent the essential information [1, 7] – indicating high redundancy and sparsity in the model’s representation. By perturbing artifacts, we mapped how and where the model encodes specific forensic cues: geometric warping and boundary blurs emerge as distinct directions in feature space (particularly in middle layers), lighting inconsistencies are picked up to a lesser degree, and color mismatches are relatively subtle until the final decision layers. In the next section, we discuss the implications of these findings and conclude with potential future work to further enhance interpretability and robustness in deepfake detection [3, 4].

**Layerwise Forensic Sensitivity.** Figure 1 ranks transformer submodules by their forensic importance scores—defined as the change in output logits in response to targeted feature interventions at each layer. Interestingly, the earliest blocks (particularly `blocks.0.attn.proj`, `blocks.0.attn`, and `blocks.0.mlp`) emerge as the most sensitive, with scores exceeding 50. These modules likely capture strong low-level cues (e.g., boundary blur, geometric distortions) crucial for deepfake detection. Sensitivity diminishes progressively in deeper layers, with top blocks like `blocks.31.*` scoring under 14. This pattern suggests that forensic signal encoding is highly front-loaded in the network, concentrated in early-to-mid representations, while deeper layers may primarily consolidate or re-encode features learned earlier. These findings validate the importance of early representations in forensic-aware transformers.

**SAE Training Progress.** Figure 2 illustrates training dynamics for the enhanced Sparse Autoencoder (SAE). The

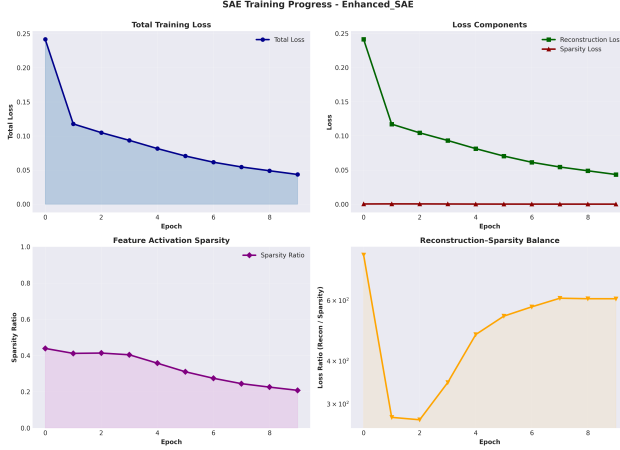


Figure 2. Training diagnostics of the enhanced SAE. Top: total loss and component breakdown; Bottom: feature sparsity trends and reconstruction-sparsity balance.

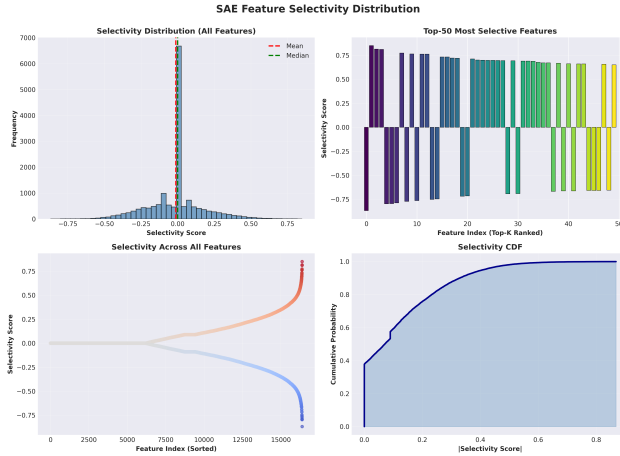


Figure 3. Selectivity profile of SAE latent features. Top-left: global distribution; Top-right: Top-50 ranked; Bottom-left: full sorted index; Bottom-right: CDF of absolute selectivity.

total loss consistently decreases over epochs, driven predominantly by reduced reconstruction error, while the sparsity penalty remains stable and low. Feature activation sparsity improves steadily, with the average ratio dropping from 44% to under 22%, indicating that fewer latent units are required per sample as training progresses. The loss balance curve (bottom-right) shows that reconstruction error dominates sparsity throughout, though the ratio stabilizes after epoch 5. This reflects a consistent trade-off: the autoencoder preserves important features while enforcing a compact and sparse representation suitable for interpretability.

**Selectivity Analysis of SAE Features.** Figure 3 summarizes how individual SAE latent features correlate with forensic artifact intensity. The selectivity distribution (top-left) is tightly centered around zero, indicating that most

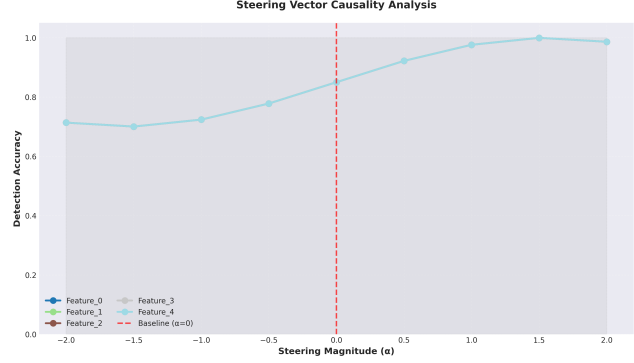


Figure 4. Causal steering of latent features. Accuracy increases with positive steering magnitude  $\alpha$ , confirming the directionality and influence of select latent units.

features are uncorrelated with artifact changes. However, a small subset exhibit high positive or negative selectivity (top-right), reflecting strong monotonic responses to artifact strength. The bottom-left panel shows this more clearly: only a few hundred out of 16,384 latent units achieve selectivity  $|\rho| > 0.5$ . The cumulative distribution (bottom-right) confirms this sparsity—over 80% of features have negligible selectivity ( $|\rho| < 0.2$ ). This reinforces that artifact-related information is concentrated in a narrow, highly selective subset of the SAE’s latent space.

**Causal Steering of Latent Features.** Figure 4 evaluates causal influence by linearly manipulating latent features via a steering vector scaled by  $\alpha$ . Steering in the positive direction ( $\alpha > 0$ ) leads to consistent improvements in detection accuracy, peaking near  $\alpha = 1.5$ , while negative steering degrades performance. This directional trend confirms that the selected features contribute causally to the model’s fake classification. Notably, performance saturates at high  $\alpha$ , suggesting that artifact-related information is already strongly encoded at moderate activation levels. These findings support the causal interpretability of SAE-identified latent axes.

**Forensic Manifold Metrics.** Figure 5 summarizes geometric properties of the latent feature manifolds under four artifact types. Intrinsic dimensionality (top-left) clusters tightly around 3–4 (mean 3.75), indicating that artifact-driven feature variation lies along low-dimensional axes. Curvature values (top-right) are moderately high (mean 19.15), suggesting nonlinear trajectories through latent space as artifact intensity increases. Feature selectivity (bottom-left) is tightly distributed near 0.495, confirming that artifacts consistently activate a focused subset of latent units. Collectively, these metrics highlight th

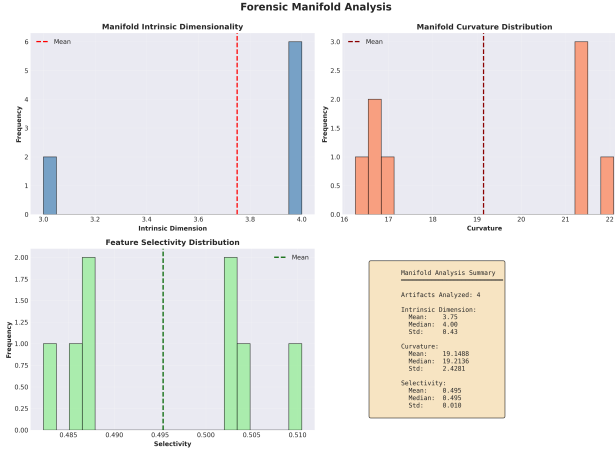


Figure 5. Distribution of forensic manifold metrics across artifact types. Includes intrinsic dimensionality (top-left), curvature (top-right), and feature selectivity (bottom-left), with summary statistics (bottom-right).

## 6. Limitation and Future Works

The study has several constraints, including its use of a small and limited dataset, reliance on synthetic artifact simulations, and focus on a single architecture. These choices help isolate forensic cues but do not fully represent the diversity or complexity of real deepfakes, especially those generated by modern or emerging methods. Some information may be lost due to sparse autoencoder compression, and the analysis does not address adversarial robustness, temporal artifacts in video, or the gap between mathematical latent features and human-understandable explanations.

Future work includes extending the framework across model architectures, adding semantic labels to latent features, and studying compound artifacts that occur together in real deepfakes. Additional goals involve improving adversarial robustness, incorporating temporal analysis for videos, building real-time explainable detection systems, and expanding to other forms of synthetic media. Human-in-the-loop validation, model attribution, and integration of ethical safeguards are also key directions for developing more reliable and socially responsible deepfake detection methods.

## 7. Conclusion

We presented a novel interpretability study of deepfake detection through the lens of mechanistic analysis, applying it to a large vision-language model. Our approach – combining sparse autoencoder feature discovery with forensic manifold analysis – enabled us to peel back the layers of a state-of-the-art deepfake detector and examine its internal logic. The results revealed that the model internally learns a highly sparse and factorized representation: only a few la-

tent features in each layer are active at once, and many neurons are tuned to specific telltale artifacts of manipulation (such as geometric warping or blurring). We quantified how these artifact-related features evolve across the network, finding that mid-level layers explicitly encode forensic artifact variations in a multi-dimensional manifold, which the final layer then collapses into the binary classification decision. These insights not only demystify the “black box” to some extent – showing, for example, that the detector looks for physically interpretable cues like misaligned geometry and blurred boundaries – but also provide guidance for future model improvements. For instance, knowing that certain artifact signals are crucial suggests that augmenting training data or architectures to enhance those signals could improve generalization to new deepfake methods. Moreover, the methodology introduced here is broadly applicable: researchers can apply our SAE + manifold analysis pipeline to other models (or other types of fake media detectors) to diagnose what features they rely on. In future work, we plan to extend this approach by linking the discovered latent features back to human-understandable concepts (e.g., via further visualizations or by generating images that activate a given neuron), and by exploring how the presence of multiple simultaneous artifacts is handled in the feature space (since real deepfakes may exhibit combinations of artifacts). We also aim to integrate these interpretability findings into the model’s output – for example, producing an explanation alongside each detection (“classified as fake due to unnatural warping and color mismatch”). We hope that this research paves the way toward deepfake detectors that are not only accurate but also transparent and trustworthy, enabling safer use of AI in detecting manipulated media.

## References

- [1] Emmanuel Ameisen, Jack Lindsey, Adam Pearce, Wes Gurnee, Nick L. Turner, Ben Chen, Chris Citro, Daniel Abrahams, Shan Carter, Ben Hosmer, Jonathan Marcus, Max Sklar, Alec Templeton, Tom Bricken, Colin McDougall, Hamish Cunningham, Tom Henighan, Adam Jermyn, Andrew Jones, Aaron Persic, Zeming Qi, Ben T. Thompson, Sam Zimmerman, Kevin Rivoire, Thomas Conerly, Chris Olah, and Joshua Batson. Circuit tracing: Revealing computational graphs in language models. *Transformer Circuits*, 2025. 6
- [2] Bartosz Cywiński, Emil Ryd, Rowan Wang, Senthooran Rajamanoharan, Neel Nanda, Arthur Conmy, and Samuel Marks. Eliciting secret knowledge from language models, 2025. 2
- [3] Joshua Engels, Elliot J. Michaud, Irene Liao, Wes Gurnee, and Max Tegmark. Not all language model features are one-dimensionally linear. In *Proceedings of the Thirteenth International Conference on Learning Representations*, 2025. 6
- [4] Luke Gorton. Curve detector manifolds in inceptionv1. 2024. 6
- [5] Wes Gurnee, Emmanuel Ameisen, Isaac Kauvar, Julius

Tarng, Adam Pearce, Chris Olah, and Joshua Batson. When models manipulate manifolds: The geometry of a counting task. *Transformer Circuits*, 2025. Accessed: 2025-12-03. 2

[6] Subhash Kantamneni, Joshua Engels, Senthooran Rajamanoharan, Max Tegmark, and Neel Nanda. Are sparse autoencoders useful? a case study in sparse probing, 2025. 2

[7] Elliot J. Michaud, Zijie Liu, Ugur Girit, and Max Tegmark. The quantization model of neural scaling. In *Proceedings of the 37th Conference on Neural Information Processing Systems*, 2023. 6

[8] Chris Olah. Interpretability dreams. 2023. 4

[9] Chris Olah. What is a linear representation? what is a multi-dimensional feature? 2024. 4

[10] Chris Olah and Joshua Batson. Feature manifold toy model. 2023. 5

[11] Rohin Shah, Alex Irpan, Alexander Matt Turner, Anna Wang, Arthur Conmy, David Lindner, Jonah Brown-Cohen, Lewis Ho, Neel Nanda, Raluca Ada Popa, Rishabh Jain, Rory Greig, Samuel Albanie, Scott Emmons, Sebastian Farquhar, Sébastien Krier, Senthooran Rajamanoharan, Sophie Bridgers, Tobi Iijito, Tom Everitt, Victoria Krakovna, Vikrant Varma, Vladimir Mikulik, Zachary Kenton, Dave Orr, Shane Legg, Noah Goodman, Allan Dafoe, Four Flynn, and Anca Dragan. An approach to technical AI safety and security, 2025. 1

[12] Lee Sharkey, Bilal Chughtai, Joshua Batson, Jack Lindsey, Jeff Wu, Lucius Bushnaq, Nicholas Goldowsky-Dill, Stefan Heimersheim, Alejandro Ortega, Joseph Bloom, Stella Biderman, Adria Garriga-Alonso, Arthur Conmy, Neel Nanda, Jessica Rumbelow, Martin Wattenberg, Nandi Schoots, Joseph Miller, Eric J. Michaud, Stephen Casper, Max Tegmark, William Saunders, David Bau, Eric Todd, Atticus Geiger, Mor Geva, Jesse Hoogland, Daniel Murfet, and Tom McGrath. Open problems in mechanistic interpretability, 2025. 1

[13] Constantin Venhoff, Iván Arcuschin, Philip Torr, Arthur Conmy, and Neel Nanda. Base models know how to reason, thinking models learn when, 2025. 1

[14] An Yang, Baosong Yang, Binyuan Hui, Bo Zheng, Bowen Yu, Chang Zhou, Chengpeng Li, Chengyuan Li, Dayiheng Liu, Fei Huang, Guanting Dong, Haoran Wei, Huan Lin, Jialong Tang, Jialin Wang, Jian Yang, Jianhong Tu, Jianwei Zhang, Jianxin Ma, Jianxin Yang, Jin Xu, Jingren Zhou, Jinze Bai, Jinzheng He, Junyang Lin, Kai Dang, Keming Lu, Keqin Chen, Kexin Yang, Mei Li, Mingfeng Xue, Na Ni, Pei Zhang, Peng Wang, Ru Peng, Rui Men, Ruize Gao, Runji Lin, Shijie Wang, Shuai Bai, Sinan Tan, Tianhang Zhu, Tianhao Li, Tianyu Liu, Wenbin Ge, Xiaodong Deng, Xiaohuan Zhou, Xingzhang Ren, Xinyu Zhang, Xipin Wei, Xuancheng Ren, Xuejing Liu, Yang Fan, Yang Yao, Yichang Zhang, Yu Wan, Yunfei Chu, Yuqiong Liu, Zeyu Cui, Zhenru Zhang, Zifang Guo, and Zhihao Fan. Qwen2 technical report, 2024. 3

## A. Enhanced Forensic Analysis Results

In this appendix, we report the structured outputs of our multistage interpretability pipeline for the Qwen2-VL-2B

deepfake detector. The results summarize (i) model and dataset configuration, (ii) layerwise forensic importance scores for selected transformer blocks, and (iii) sparse autoencoder statistics and downstream analysis metadata.

### A.1. Experiment Configuration

Parameter	Value
Base model	Qwen/Qwen2-VL-2B-Instruct
# real samples	250
# fake samples	250
SAE latent dimension	16,384
Extended thinking	Enabled (true)

Table 1. Configuration used for the enhanced interpretability pipeline.

### A.2. Stage 1: Layerwise Forensic Importance Scores

Table 2 and Table 3 report the forensic importance scores (change in output logits under targeted interventions) for attention and MLP submodules across selected visual transformer blocks.

Block	Submodule	Score
0	Attn.proj	50.38
0	Attn	50.36
0	MLP	45.63
6	Attn.proj	38.31
6	Attn	38.27
6	MLP	37.33
12	Attn.proj	29.59
12	Attn	29.53
12	MLP	28.27

Table 2. Stage 1 forensic importance scores for early and mid-layer blocks.

### A.3. Stage 2: Sparse Autoencoder Statistics

Stage 2 trains an under-complete sparse autoencoder over the selected layer activations. Global summary statistics are:

- Mean sparsity of SAE latent codes: 0.208 (fraction of active latent units).
- Mean selectivity to forensic artifacts: 0.117 (average absolute correlation).

These values confirm that the SAE learns a compact, highly sparse representation while preserving artifact-sensitive structure in the latent space.

Block	Submodule	Score
18	Attn.proj	27.90
18	Attn	27.96
18	MLP	26.62
24	Attn.proj	28.18
24	Attn	28.20
24	MLP	27.20
31	Attn.proj	13.49
31	Attn	13.47
31	MLP	12.02

Table 3. Stage 1 forensic importance scores for deeper visual blocks.

#### A.4. Stage 2b: Artifact Manifold Enumeration

In Stage 2b, we enumerate and analyze manifolds corresponding to distinct forensic artifact types. The current configuration models:

- Number of artifact types: 4
  - Geometric warp
  - Lighting inconsistency
  - Boundary blur
  - Color mismatch

#### A.5. Stage 3: Steering Curve Extraction

Stage 3 fits steering directions over SAE latent units to study causal feature manipulation. In this experiment:

- Number of steering curves extracted: 5

These curves are used to generate plots of detection accuracy as a function of steering magnitude, as discussed in the main text.

#### A.6. Stage 4: Extended Thinking Status

Finally, Stage 4 records the status of extended interpretability routines:

- Extended-thinking pipeline: successfully completed (true).

This completion flag indicates that all four stages of the enhanced analysis were run end-to-end for the reported configuration.